Springer

KSME

Journal of Mechanical Science and Technology 24 (7) (2010) 1451~1463
www.springerlink.com/content/1738-494x
DOI 10.1007/s12206-010-0421-5

Fluid-particle interaction simulations of the interception of red blood cells in shear flow †

Choeng Ryul Choi[1] and Chang Nyung Kim[2,3,*]

[1]*Department of Mechanical Engineering, College of Engineering, Kyung Hee University, Yongin-si, 446-701, Korea*
[2]*College of Engineering, Kyung Hee University, Yongin-si, 446-701, Korea*
[3]*Industrial Liaison Research Institute, Kyung Hee University, Yongin-si, 446-701, Korea*

(Manuscript Received January 11, 2010; Revised March 16, 2010; Accepted March 25, 2010)

Abstract

Numerical simulations of the motion of red blood cells (RBCs) freely suspended in shear flow have been successfully performed to investigate the nature of pairwise interception of RBCs using a fluid-particle interaction method based on the arbitrary Lagrangian-Eulerian (ALE) method and a dynamic mesh method. The applicability of the interaction method that we used was validated by comparing the simulation results with an analytical solution for an elliptical particle in shear flow. We found that positive and negative transverse shifts of the RBCs take place during the interceptions, yielding a non-zero RBC self-diffusivity, and that a phase shift occurs during the rotating behavior and lasts even after the separation. The behaviors of the approaching RBCs are adjusted by interactions with the surrounding flow fields during interception. The pressure between a pair of RBCs causes either an attractive or repulsive force. The nature of the pairwise interception is influenced not only by the flow fields but also by kinematic characteristics (i.e., instantaneous translational and rotational behavior) of the two RBCs.

Keywords: Fluid-particle interaction; Interception; Red blood cells (RBCs); Self-diffusivity

1. Introduction

In fluid-particle suspension problems frequently observed in physical and biological sciences, the interaction between the fluid and particles may affect the viscosity and rheological behavior of the suspension. It is known that the clusters and anisotropic particle micro-structures are the result of particle migrations produced by particle–particle and particle–wall interactions [1-4]. A well-known example of a fluid-particle interaction at the mesoscopic scale is the dynamics of red blood cells (RBCs). In microcirculation, the flow behavior of RBCs plays a crucial role in many physiological and pathological phenomena. For example, the random-like transverse motion and rotation of RBCs in shear flow is believed to play an important role in thrombogenesis [5]. These motions are strongly related to RBC to RBC interactions as well as fluid (plasma) to RBC interactions, since one RBC is intercepted by another approaching from above or below.

The dynamics of a single ellipsoidal particle in shear flow and the rheology of an infinitely dilute suspension were first considered by Jeffery [6] who showed that the particle director gyrates along a closed orbit that is determined by initial conditions. Subsequently, a number of analytical studies have tried to explain observed phenomena and model them mathematically [7-10]. The rheological properties and micro-structure dynamics of suspensions with spherical particles have also been extensively investigated experimentally, theoretically and numerically via simulations at low and moderate volume fractions [11-14]. In contrast, investigations of suspensions with non-spherical particles are rare due to their more complicated dynamics [15-19]. Recently, the effect of the aspect ratio of elliptical particles on the statistics of particle orientation and effective viscosity of a non-dilute suspension in simple shear flow has been studied by dynamic simulations based on an improved implementation of the boundary-element method for particulate Stokes flow [20]. The results show that the effective viscosity decreases as the particles become more elongated, and the transition to the nematic state is expected to occur gradually rather than abruptly at a critical areal fraction. In a dilute suspension, Pozrikidis [21] simulated the interception of two ellipsoidal particles in simple shear flow directly by solving an integral equation of the second kind arising from the double-layer representation for Stokes flow. Although numerical simulations have helped elucidate the hy-

† This paper was recommended for publication in revised form by Associate Editor Haecheon Choi

*Corresponding author. Tel.: +82 31 201 2578, Fax.: +82 31 202 9715
E-mail address: cnkim@khu.ac.kr

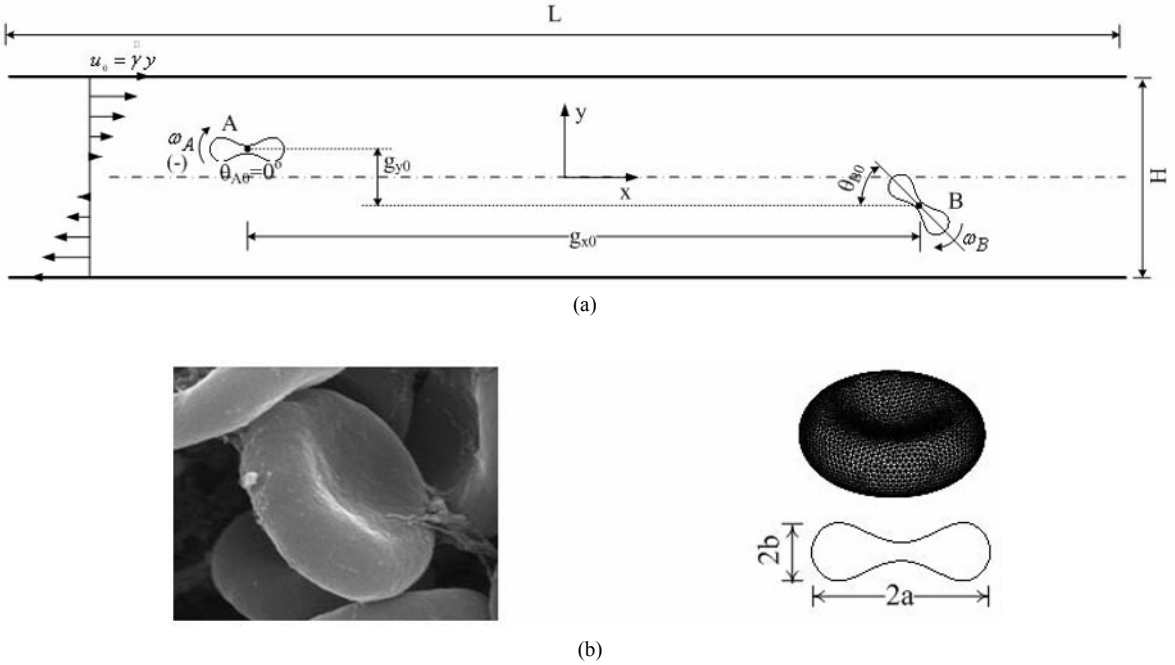

(a)

(b)

Fig. 1. (a) Schematic illustration of the interception of RBCs initially placed away from the *x* axis in shear flow. (b) Shape of an unstressed RBC (a = 3.91 μm, b = 1.283 μm).

drodynamics of the microstructure and rheology of homogeneous suspensions of spherical or ellipsoidal particles, simulations of the motion of particles with arbitrary shapes (e.g., RBCs with a biconcave discoid shape) in an effectively infinite or confined domain still remain an important challenge due to the lack of efficient and accurate numerical methods.

To investigate the nature of pairwise interception in this work, the interceptions of RBCs in a dilute suspension in simple shear flow are simulated in a two-dimensional system with emphasis on the net particle displacement and shift in the rotation phase. To include the hydrodynamic interaction between the fluid (plasma) and RBCs, a fluid-particle interaction method (or fluid-structure interaction method: FSI) is developed based on the arbitrary Lagrangian-Eulerian (ALE) method and a dynamic mesh method. In this method, the equations for the fluid flow and RBCs motion are sequentially solved in a two-way coupling fashion and the overall calculation procedure is entirely implemented by a fluid-particle interaction algorithm.

2. Problem description

Consider a homogeneous, dilute, mono-dispersion of RBCs in motion in a linear shear flow. On occasion, one RBC can be intercepted by another. To simulate the interception of a pair of RBCs in a linear shear flow, a flow channel with two parallel plates is considered as shown in Fig. 1. The height of the channel, H, is 25 μm and the length, L, is 100 μm. Initially, the plates are at rest and the flow between the plates is stationary. A pair of RBCs, assumed to be neutrally buoyant, is symmetrically placed in the channel with respect to the origin. The first labeled A is placed at the left above the *x* axis and the other, labeled, B is placed at the right below the *x* axis. The two RBCs are separated by g_{x0} and g_{y0} in the *x* and *y* directions, respectively. The RBCs are biconcave representing an unstressed RBC shown in Fig. 1(b). The three-dimensional shape of the RBC is obtained from the following formula [22-23]:

$$y = \pm R_0 \sqrt{1-\frac{(x^2+z^2)}{R_0^{\,2}}}\left[c_0 + c_1\frac{(x^2+z^2)}{R_0^{\,2}} + c_2\left(\frac{(x^2+z^2)}{R_0^{\,2}}\right)^2\right]$$

where R_0 is 3.91 μm, and c_0, c_1 and c_2 are 0.1035805, 1.001279, and -0.561381, respectively. In the present two-dimensional simulations, the central cross section of this shape is considered.

As the simulation begins, the upper plate moves right at a constant velocity, $u_0 = \dot{\gamma}(H/2)$, while the lower one moves in the opposite direction at the same speed. A linear shear flow at the shear rate $\dot{\gamma} = 2u_0/H$ will develop inside the channel. RBC A will begin to move right and rotate clockwise due to the linear shear flow. RBC B, on the other hand, will begin to move left and rotate clockwise. As time progresses, the two RBCs will approach each other.

When the approaching RBCs encounter each other, it is hard to predict whether they will collide or just pass closely and how the interception affects each RBC's behavior since it depends on both the RBC-RBC interaction and the fluid-RBC interaction. Specific outcomes will depend on several parameters such as the distance between the RBCs, inclination angles and shear rates in the channel as mentioned by Pozrikidis [21]. To evaluate the effects of these parameters on the characteristics of RBC interception, several simulations are carried out using different initial conditions such as initial vertical gaps and inclination angles.

In this study, the fluid confined between the two parallel plates (which models human blood plasma) is assumed to be an incompressible and Newtonian viscous fluid. Its density and viscosity are ρ_f = 1,060 *kg/m*^{3} and μ = 1.2 *cp*, respectively [24]. The RBCs are assumed to be non-deformable.

3. Numerical methods

3.1 Numerical methods

The problem considered can be approximated as a fluid-particle interaction problem where the fluid phase is blood plasma and the rigid particles are RBCs. In such problems, the flow of an incompressible and Newtonian viscous fluid is governed by the continuity and Navier-Stokes equations.

$$\nabla \cdot \vec{v} = 0 \tag{1}$$

$$\rho_f \left(\frac{\partial \vec{v}}{\partial t} + \vec{v} \cdot \nabla \vec{v} \right) = -\nabla p + \mu \nabla^2 \vec{v} \tag{2}$$

where ρ_f is the fluid density, $\vec{v}$ is the flow velocity, p is the pressure, and μ is the molecular viscosity of the fluid.

The suspended rigid particle satisfies Newton's second law for translational motion and the Euler equations for rotation.

$$m_p \frac{d\vec{V}_p}{dt} = \vec{F} \tag{3}$$

$$I \frac{d\vec{\omega}_p}{dt} = \vec{T} \tag{4}$$

where m_p is the mass of the particle and I is the moment of inertia matrix of the particle. $\vec{V}_p$ and $\vec{\omega}_p$ are the translational and angular velocities of the particle. The hydrodynamic force $\vec{F}$ and moment $\vec{T}$ acting on the particle are obtained by integrating the fluid stress over the particle surface. The centroid $\vec{X}_p$ and the orientation $\vec{\theta}_p$ of the particle are updated according to the following equations.

$$\frac{d\vec{X}_p}{dt} = \vec{V}_p \tag{5}$$

$$\frac{d\vec{\theta}_p}{dt} = \vec{\omega}_p \tag{6}$$

The no-slip condition is satisfied on the particle boundary. The velocity at a point of the particle can be expressed in the following equation;

$$u = \vec{V}_p + \vec{\omega}_p \times (x - \vec{X}_p) \tag{7}$$

3.2 Dynamic mesh updating methods

The translation and rotation of the particle interacting with the fluid flow cause a change in the mesh system in the ALE approach. To implement this change, the finite element mesh system initially designed is deformed or re-meshed in accordance with the moving particle by the dynamic mesh method (FLUENT documentation, ANSYS, USA) [25]. The deforming mesh is of a spring-based method which allows a robust mesh deformation under the assumption that the mesh element edges behave like an idealized network of interconnected springs. The re-meshing is adopted to properly treat degenerated cells through the agglomeration of cells that violate a given skewness criterion (< 0.8) and the local partition of the agglomerated cells. The mesh is locally updated with new cells satisfying the skewness criterion where the solutions are interpolated from those based on the old cells at the beginning of each FSI sub-iteration loop.

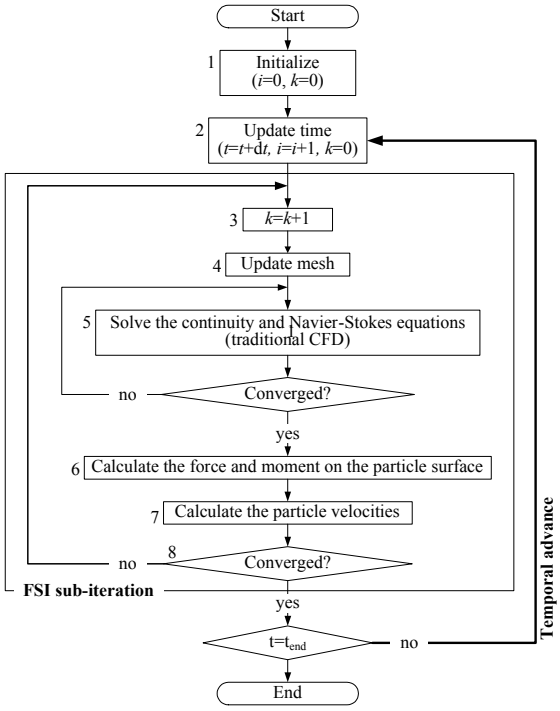

Fig. 2. Simplified fluid-particle interaction algorithm developed in the present work (*i*: time step index, *k*: FSI iteration index at the *i*th time step).

3.3 Fluid-particle interaction algorithm

The interaction between fluid flow and particle motion is implemented through an FSI method based on the ALE method and the dynamic mesh method addressed above. The governing equations for the fluid and particles are iteratively sequentially solved until the solutions converge in a two-way coupling fashion for strong fluid–structure interactions at a given time step and then the calculation proceeds to the next time step. The overall calculation procedure of the FSI method is depicted in Fig. 2, where *i* is the time step index and *k* denotes the index of the FSI sub-iteration at the *i*th time step, which can be outlined as follows:

Step 1. Simulation control variables are set to $i = 0$ and $k = 0$. The materials properties (ρ_f, ρ_p and μ) are set and all flow variables $\vec{u}_i$ and p_i are initialized. The particle

velocities $\vec{V}_i^k$ and $\vec{\omega}_i^k$ are also initialized.

Step 2. The time is updated to $t = t + \Delta t$. $i = i + 1$ and $k = 0$.

Step 3. $k = k + 1$.

Step 4. The mesh is updated in accordance with the moving particles by the dynamic methods.
If $k = 1$, based on $\vec{V}_{i-1}^{\,last}$ and $\vec{\omega}_{i-1}^{\,last}$.
If $k \neq 1$, based on $\vec{V}_i^{k-1}$ and $\vec{\omega}_i^{k-1}$.
The superscript *last* indicates the final value calculated at the previous time step (i-1 th).

Step 5. Using the particle velocities (if k = 1, $\vec{V}_{i-1}^{\,last}$ and $\vec{\omega}_{i-1}^{\,last}$ / if $k \neq 1$, $\vec{V}_i^{k-1}$ and $\vec{\omega}_i^{k-1}$) as the boundary conditions, the velocity $\vec{u}_i$ and pressure p_i are obtained by solving the governing equations Eqs. 1 and 2 in the updated mesh by a usual CFD method.

Step 6. The hydrodynamic force $\vec{F}_i^k$ and moment $\vec{T}_i^k$ acting on the particle are obtained by integrating the fluid stress over the particle surface.

Step 7. The velocities of the particle $\vec{V}_i^k$ and $\vec{\omega}_i^k$ are calculated with a backward Euler scheme as follows.

$$\begin{aligned} \dot{\vec{V}}_i^{\,k} &= \dot{\vec{V}}_i^{\,k-1} + w\left(\frac{\vec{F}^k}{m} - \dot{\vec{V}}_i^{\,k-1}\right) \\ \dot{\vec{\omega}}_i^{\,k} &= \dot{\vec{\omega}}_i^{\,k-1} + w\left(\frac{\vec{T}^k}{I_i^k} - \dot{\vec{\omega}}_i^{\,k-1}\right) \end{aligned} \tag{8}$$

$$\begin{aligned} \vec{V}_i^k &= \vec{V}_{i-1}^{\,last} + \dot{\vec{V}}_i^{\,k} \cdot \Delta t \\ \vec{\omega}_i^{\,k} &= \vec{\omega}_{i-1}^{\,last} + \dot{\vec{\omega}}_i^{\,k} \cdot \Delta t \end{aligned} \tag{9}$$

where $\dot{\vec{V}}$ and $\dot{\vec{\omega}}$ are the translational and angular accelerations of the particle, respectively. w is an under-relaxation factor which plays a role in damping changes in the predicted values during the FSI sub-iteration. In Eq. 8, if k = 1, $\dot{\vec{V}}_i^{\,k-1} = \dot{\vec{V}}_{i-1}^{\,last}$ and $\dot{\vec{\omega}}_i^{\,k-1} = \dot{\vec{\omega}}_{i-1}^{\,last}$.

Step 8. Convergence is checked. If $\left|\left((\vec{F}^k/m) - \dot{\vec{V}}_i^{\,k-1}\right)/\dot{\vec{V}}_i^{\,k-1}\right|$ and $\left|\left((\vec{T}^k/I_i^{\,k}) - \dot{\vec{\omega}}_i^{\,k-1}\right)/\dot{\vec{\omega}}_i^{\,k-1}\right|$ are less than a given tolerance, ε, the calculation proceeds to the next time step and is restarted at step 2. If not, another FSI sub-iteration is started so that steps 3 to 7 are repeated with the values predicted at the previous FSI sub-iteration until a given convergence criterion is satisfied.

Step 9. The above steps are continued until the time reaches the end time.

In the present simulations, the mesh update at Step 4 is implemented by the dynamic mesh method with the use of FLUENT and the calculation of the flow field at Step 5 is carried out by solving the continuity and Navier-Stokes equations in the usual CFD method. The overall calculation procedure is handled by an external FSI code based on the above algorithm. Since the use of FLUENT is not compulsory for the implementation of the above FSI method, it can be replaced with another general fluid flow solver.

3.4 Numerical schemes

Clear original figures in black and white should be used. Equations should be numbered consecutively throughout the paper and located at the right margin as in Eq. (1) below. Figures and tables should be placed at the top or at the bottom of each column as in Fig. 1 and Table 1.

The mesh system in the current study consists of about 12,000 triangular cells with refined meshes in the vicinity of the RBCs. Tests for grid size dependence with the current mesh system and several different mesh systems with approximately 7,000 - 15,000 cells have shown that the current mesh system provides sufficient mesh-independent solutions. During simulations, the number of cells in the mesh system varies since the meshes can be re-meshed by the dynamic mesh method in association with particle motions.

Periodic boundary conditions are imposed at both end sides. For the upper and lower walls, constant velocity conditions ($u_0 = \dot{\gamma}(H/2)$) are set to generate a shear flow. Note that the shear rate in the channel is $\dot{\gamma} = 1\,s^{-1}$ in all simulations of this study. The choice of the size of the time step can be influential to the result and the stability of simulation. After several preliminary simulations with different time step sizes, a range of time steps from 0.005 s to 0.025 *s* was chosen to avoid adverse impacts on results, achieve reasonable computation time, and retain stable simulations.

In the present simulations, FLUENT was used to solve the governing equations for fluid flow. A second-order upwind scheme was used to treat the convective terms and a backward first order implicit scheme was employed for the time integration of the fluid flow. The PISO (pressure-implicit with splitting of operators) algorithm was used for pressure-velocity coupling.

Calculations were carried out on a clustering computer with eight Quad-Core 2.5 GHz CPUs; one time step took about 50 *s*. At a given time step, convergence was achieved within five FSI sub-iterations.

4. Results and discussions

4.1 Validation of the numerical methods

To validate the numerical methods, a simple fluid-particle interaction problem where an ellipsoid is suspended in shear flow as shown in Fig. 3 is considered. Such a problem was first mathematically considered by Jeffery [6] and the following equation of the flipping velocity under the assumption of the Stokes flow was first given by Keller [26].

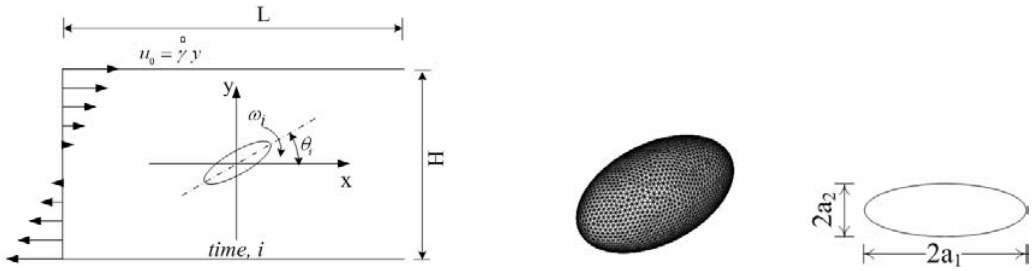

(a) (b)

Fig. 3. (a) Schematic illustrations of the dynamics of an ellipsoidal single cell for the validation of the used numerical methods. (b) 2D and 3D shapes of an ellipsoid (a_1 = 3.91 μm, a_2 = 1.11 μm). The aspect ratio is defined as $e = a_1/a_2$.

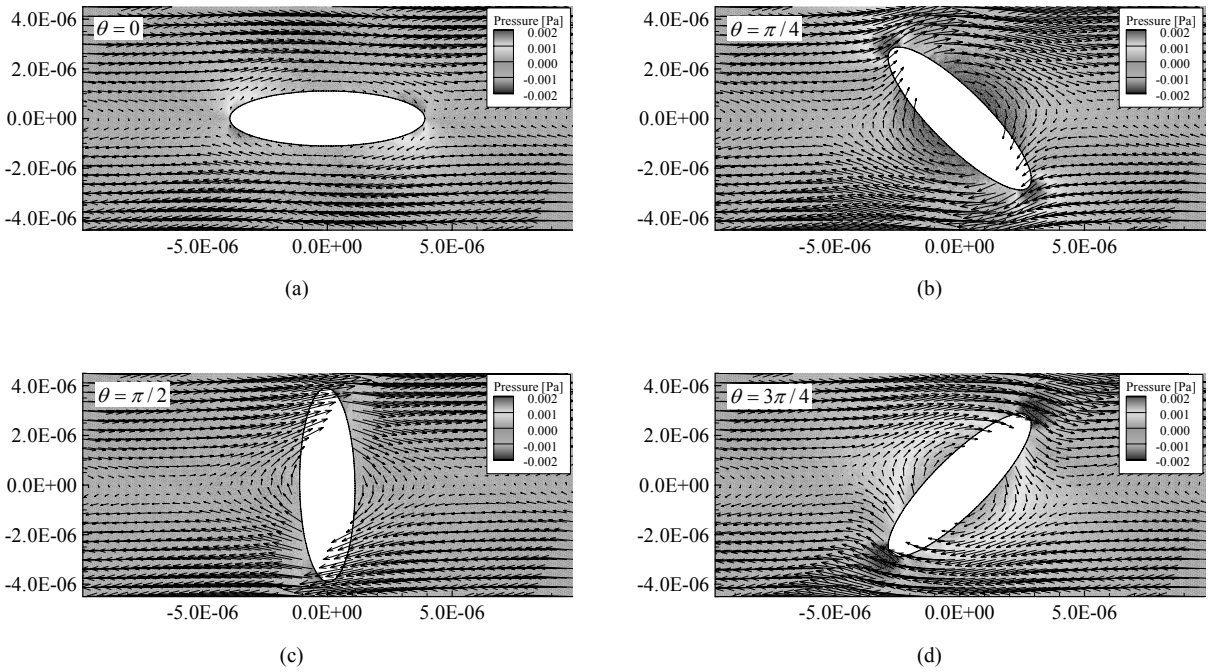

(a) (b) (c) (d)

Fig. 4. A sequence of velocity vectors and pressure distributions around the elliptical particle.

$$\frac{d\theta}{dt} = A + B\cos(2\theta) \tag{10}$$

$$\text{where} \quad A = -(\frac{1}{2}\dot{\gamma} + \frac{2a_1a_2}{{a_1}^2 + {a_2}^2}\upsilon), \quad B = \frac{1}{2}\dot{\gamma}\frac{{a_1}^2 - {a_2}^2}{{a_1}^2 + {a_2}^2} \tag{11}$$

where θ is the inclination angle of the particle with respect to the x axis and $\dot{\gamma}$ is the shear rate. v, a parameter having the dimensions of frequency, is 0 for the rigid ellipsoid (non-tank-treading) considered in this simulation and is described by a more complicated expression for a deformable ellipsoid (for detailed expression, refer to Keller and Skalak [7]). Analytically solving the ordinary differential equation Eq. 10, we obtain the time evolution of the particle inclination angle as follows.

$$\theta(t) = \text{atan}\left(\frac{A+B}{\sqrt{B^2 - A^2}}\tanh\left(\sqrt{B^2 - A^2}\,(t + t_0)\right)\right) \tag{12}$$

$$T = 2\pi/\sqrt{B^2 - A^2} \tag{13}$$

where t_0 is the time at which $\theta = 0^o$ and T is the period of the particle rotation.

In the 2D simulation for validation, an ellipse with an a_1 = 3.91 μm semi-major axis and an a_2 = 1.11 μm semi-minor axis corresponding to e = 3.52 is considered as the suspended particle. The two- and three-dimensional shapes of the ellipsoid, as seen in Fig. 3(b), have been frequently considered instead of the real RBC shape in several studies [27-29].

As the upper and lower plates begin to move, a linear shear flow is quickly developed inside the channel. With the linear shear flow the particle rotates by interacting with the surrounding fluid flow and executes a periodic rotation. A time sequence of velocity vectors and pressure distributions is shown in Fig. 4. As the major axis of the particle is parallel to the x axis, a smooth flow pattern conforming to the particle

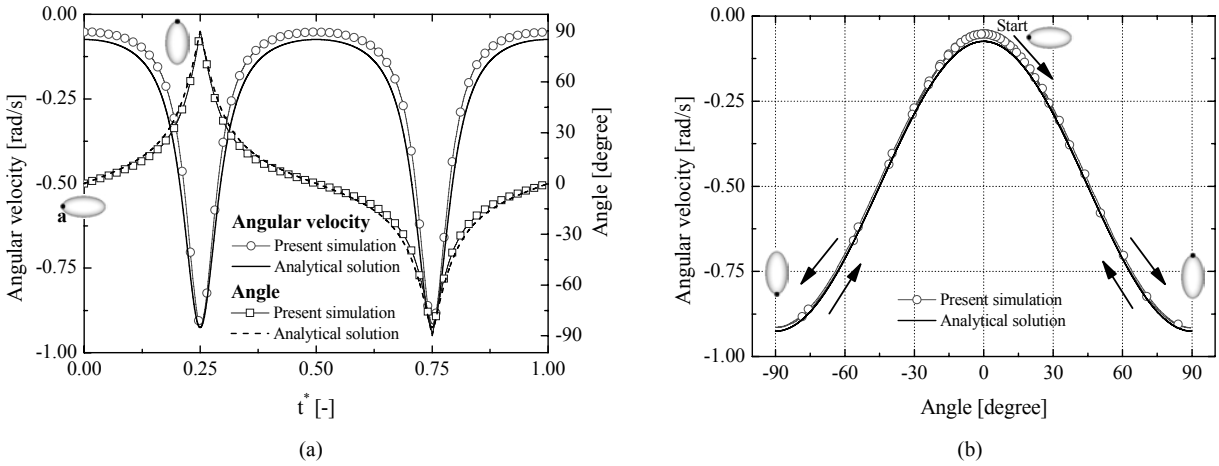

Fig. 5. Comparison between the present validation simulation and mathematical analysis for one rotation. (a) Variations of the angular velocities and inclination angles. (b) The angular velocities with the inclination angles. t^* indicates the non-dimensional time normalized by the predicted rotation period of each case (28.35 *s* for the simulation and 23.93 *s* for the analysis). The inclination angle is the acute angle with respect to the *x*-axis, and a positive sign represents that the point '*a*' exists above the center of the particle. A negative sign in the angular velocity indicates the clockwise direction.

shape is observed as shown in Fig. 4(a). But, when the inclination angle is considerable, the disturbance caused by the rotating particle is significant as presented in Fig. 4(b, c and d). Because the suspended particle executes a periodic rotating motion, a certain point on the particle surface periodically experiences high and low pressures. Such a periodic pressure distribution plays an important role in the characteristics of the particle rotation. For example, when the inclination angle is θ = 0 °, the difference in the pressure between the upper and lower parts of the left surface tends to suppress the particle rotation. When the inclination angle is considerable (for $|\theta| > \pi/4$), the difference in the pressure between the left and right parts of the upper surface supports the particle rotation.

The results from the present simulation and the mathematical analysis (Eqs. 10-12) shown in Fig. 5 clearly depict the periodic behavior of a particle suspended in the shear flow. As the long axis of the particle is parallel to the *x* axis as shown in Fig. 4(a), the particle slowly rotates due to the counterclockwise moment caused by the pressure. But, as the inclination angle increases, the angular velocity also increases and reaches a maximum at around $t^* = 0.25$ ($\theta = \pi/2$). Subsequently, the angular velocity decreases gradually. This behavior is consistent with Jeffery's results [6] where the particle axis executes a periodic rotating motion. The present simulation predicts a rotation period of 28.35 *s*, while the rotation period calculated from Eq. 13 is 23.93 *s*. The difference between the two periods is a result of a small difference in the angular velocities at $|\theta| < \pi/6$. This discrepancy in the angular velocities probably results from an inaccuracy in association with the Stokes flow approximation employed in the analytical solution procedure. This suggests that the advective inertial forces in the present fluid-particle interaction problem are not negligible. In the lump, the present validation simulation confirms that the employed numerical methods are applicable to fluid-particle interaction problems.

4.2 Behavior of a single RBC

To figure out the dynamics of a single RBC, three simulations are carried out for a single RBC placed in shear flow. In each simulation, only the RBC labeled A in Fig. 1 is considered. The three different initial centers of the RBCs in the simulations are (x_0 , y_0) = (-35 μm, 1.76 μm), (x_0 , y_0) = (-35 μm, 2.64 μm) and (x_0 , y_0) = (-35 μm, 3.91 μm).

During the simulations, the upper and lower plates move at a constant velocity and a shear flow is generated inside the channel. As seen in Fig. 6(a), the RBC moves in the *x* direction and rotates clockwise about its center due to the fluid-RBC interaction. A slight transverse displacement of the RBC in the *y* direction is observed as it moves to the right with tumbling in the flow channel as shown in Fig. 6(a). When displaced by Δx = 70 μm in the *x* direction, the RBCs in the three cases are shifted in the *y* direction by Δy = 1.03 μm, 0.78 μm and 0.66 μm, respectively, and are rotated by $\Delta\theta$ = 532 °, 367 ° and 258 °, respectively. As a result of the transverse movement, the *x*-directional velocity of the RBC center generally increases during traveling, as shown in Fig. 6(b). The *x*-directional velocity in the linear shear flow without the RBC is expressed to be $v(x_i, y_i)_i = \dot{\gamma} y_i$, as depicted in Fig. 6(b) where (x_i , y_i) denotes the position of the RBC center at a time *i.* The *x*-directional velocities of the RBC center predicted in the simulation are higher than those calculated from $v(x_i, y_i)_i = \dot{\gamma} y_i$ at any time. As the RBC translates and rotates by interacting with the surrounding fluid flow, the fluid velocity vectors and pressure distribution in the vicinity of the RBC change with time as shown in Fig. 6(c and d). As seen in the above, the force and moment on the surface of the RBC exerted by the shear stress and pressure govern the overall behavior.

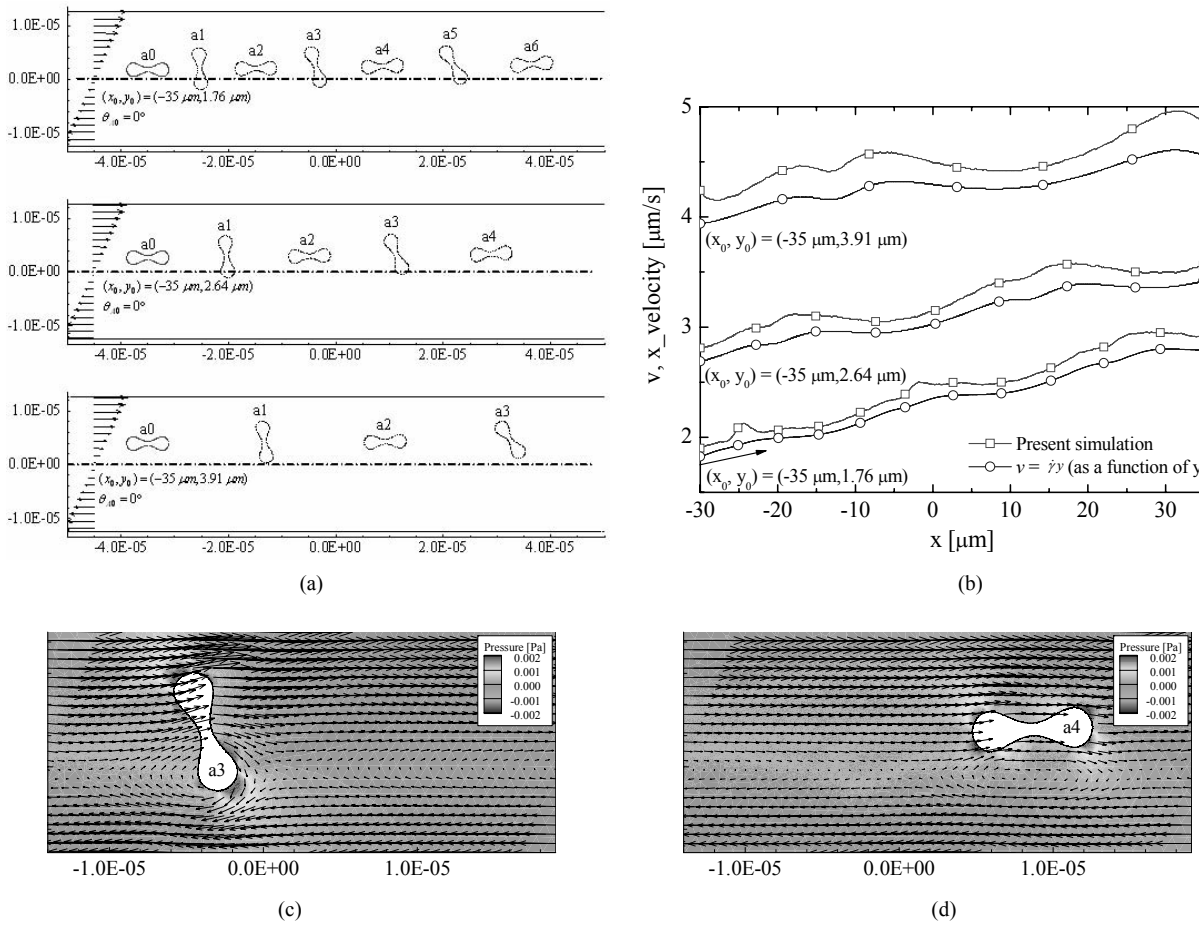

Fig. 6. Time sequence of evolving configurations of a single RBC which is initially placed away from the x axis in shear flow. (a) A time sequence of evolving configurations. The initial configuration is drawn as a red line with a notation of *a0*. The time interval is $t^* = \dot{\gamma}t = 5$. (b) Comparison of the x-directional velocities of the RBC evaluated from the present simulation and $v(x_i, y_i)_i = \dot{\gamma} y_i$. $v(x_i, y_i)_i = \dot{\gamma} y_i$ is the x-directional velocity evaluated at the point corresponding to the RBC center in the linear shear flow at the shear rate $\dot{\gamma} = 1\, s^{-1}$ at a time i. (c) and (d) are velocity vectors and pressure distributions at the instants of *a3* and *a4* in the snapshot of the simulation with (x_0 , y_0) = (-35 μm , 1.76 μm) in (a).

4.3 Interception of RBCs

Interceptions of a pair of RBCs in three different cases are simulated in the configurations shown in Fig. 1 and Fig. 7, where *a0* and *b0* denote the initial positions of the two RBCs labeled A and B, respectively. The two RBC centers are initially separated by a distance of g_{x0} = 70 μm in the x direction in all the three cases, while the initial distances in the y direction are g_{y0} = 3.53, 5.28 and 7.82 μm, respectively. The long axis of the RBCs in the three cases is initially adjusted to be parallel to the x axis, that is, $\theta_{A0} = \theta_{B0} = 0$ º.

A sequence of evolving motions during the interception is depicted in Fig. 7. In each module (a, b and c) of Fig. 7, the upper left figure shows the evolving motions with a non-dimensional time interval of $t^* = \dot{\gamma}t = 5$, while the other three snapshots depict the flow fields when a pair of RBCs are approaching each other with clockwise rotation (upper right), are closest to each other near $x = 0$ (lower left) and are getting far from each other (lower right), respectively. These figures clearly illustrate the interception process of a pair of RBCs. In all the cases, the RBCs pass close to each other without collision, and are of point symmetry with respect to the origin of the axes, while the inclination angles in the three cases are the same at a given time point. In all the cases, the closer the two RBCs are, the more different the velocity vectors and pressure distributions in the vicinity of the RBCs are from those in the simulations with a single RBC (shown in Fig. 6(c and d)). Consider the three snapshots (the lower left in the three cases) showing the flow field at the instant when the RBC centers are closest in each case in Fig. 7. The pressure pattern between the two RBCs with g_{y0} = 3.53 μm is similar to that in the case with g_{y0} = 7.82 μm in that a generally higher pressure is generated, but is quite different from that found with g_{y0} = 5.28 μm where a generally lower pressure is found. This is true even though the two RBCs in the case with g_{y0} = 7.82 μm at this instant are more separated than those in the case with g_{y0} = 5.28 μm. The above is attributed to the fact that the inclination angles and kinematic characteristics when g_{y0} = 3.53 μm are more similar to those when g_{y0} = 7.82 μm rather than those when g_{y0} = 5.28 μm. This shows that the flow field is influenced

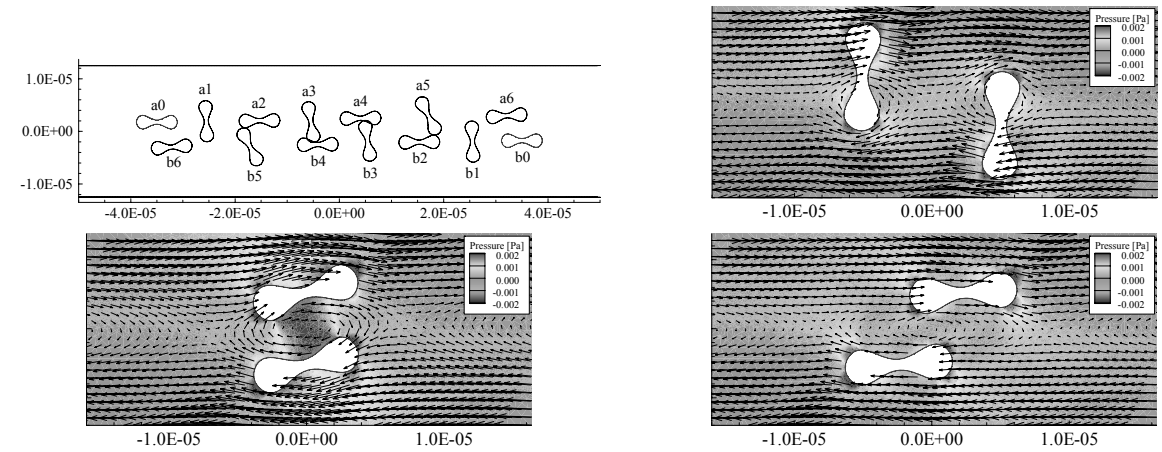

(a)

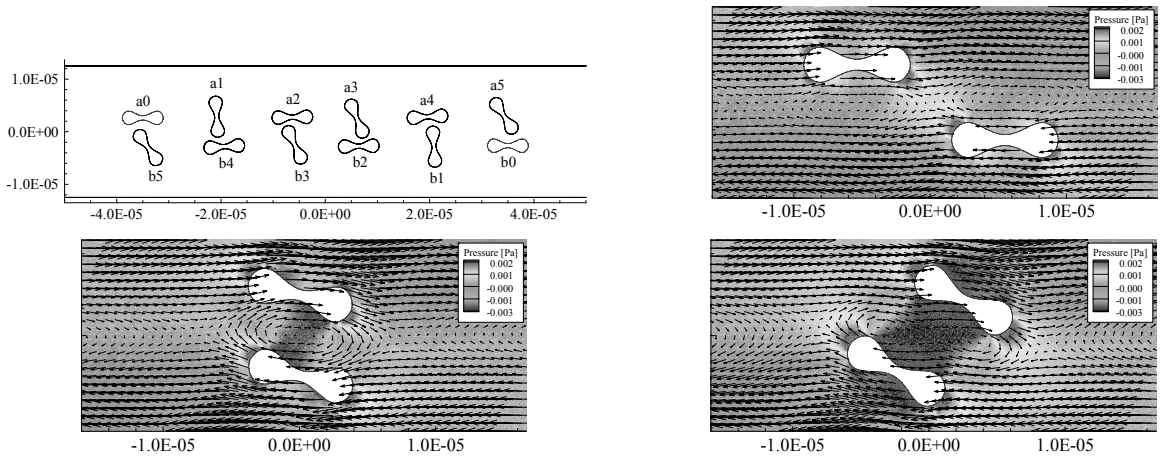

(b)

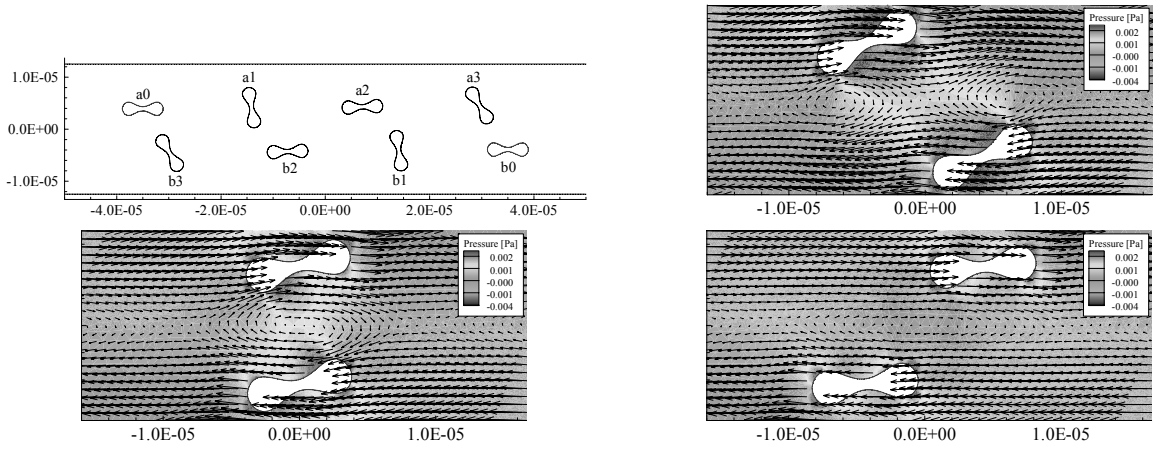

(c)

Fig. 7. Time sequence of evolving configurations of three pairs of the RBCs with different initial gaps (g_{y0}). (a) g_{y0} = 3.53 μm, (b) g_{y0} = 5.28 μm, and (c) g_{y0} = 7.82 μm. The RBCs have the same initial inclination angle of $\theta_{A0} = \theta_{B0} = 0$. The first figures show configurations at an interval of $t^* = \dot{\gamma}t$ = 5. The initial configurations are drawn as red and blue lines with notations *a0* and *b0* for RBC A and B. The other snapshots show the velocity vectors and pressure distributions when the two RBC centers are approaching each other, are closest, and are receding from each other, respectively ((a): $t^* = \dot{\gamma}t$ = 15.23, 18.23 and 19.23, (b) t^* = 10.41, 12.41 and 13.41, (c) t^* = 7.33, 8.33 and 9.33).

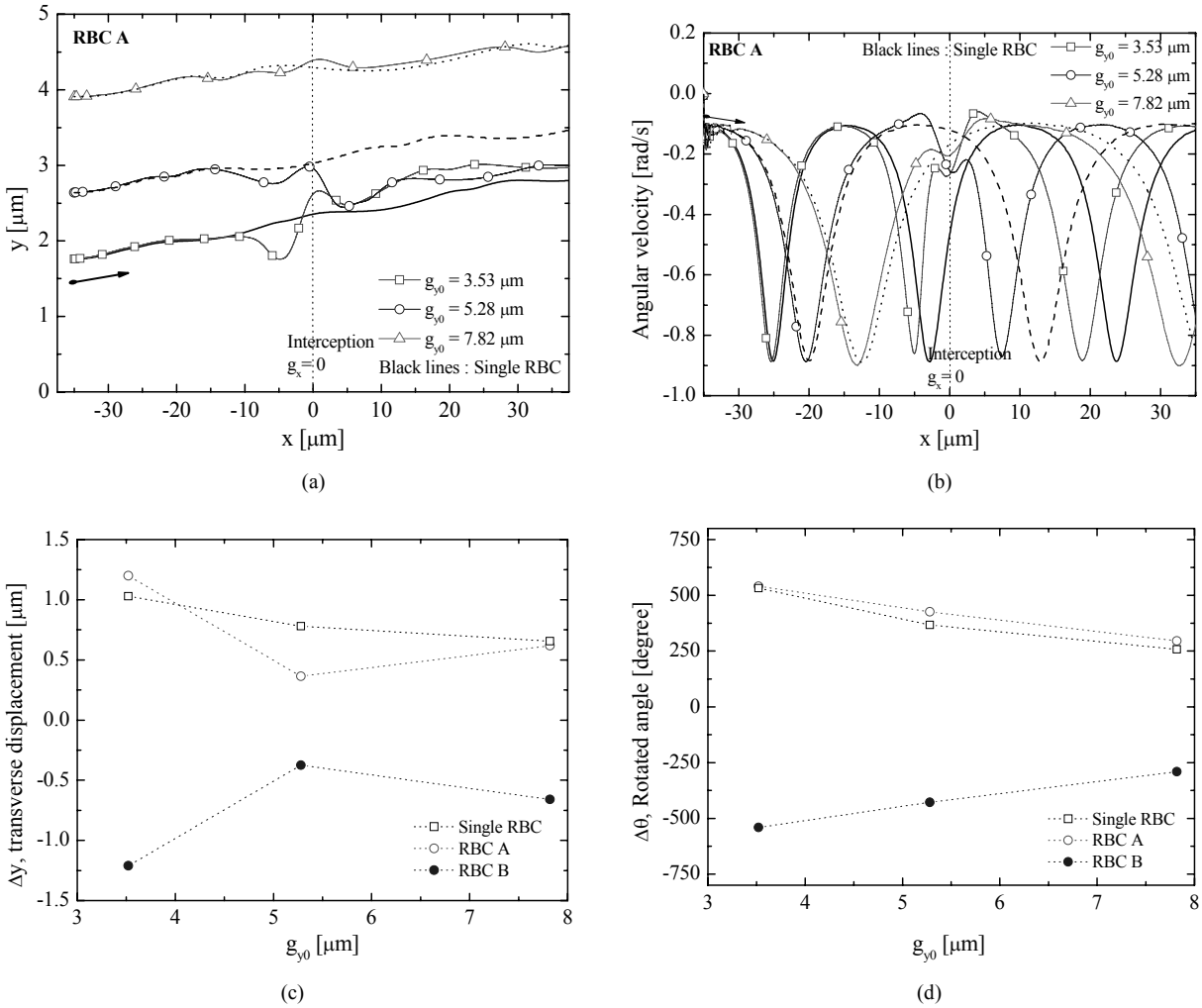

Fig. 8. Behavior of the three pairs of RBCs intercepting with different initial gaps (g_{y0}). (a) Trajectories of the centers of the RBCs. (b) Variations of the angular velocities of RBC A. (c) and (d) are net transverse displacements and rotated angles, respectively, after the RBCs are displaced by 70 μm along the x axis.

by the inclination angle of the RBCs at the time of grazing in association with the clockwise angular velocity as well as the distance between the two RBC centers at a certain instant.

The trajectories and angular velocities of one RBC (denoted by the RBC A) of the pair are shown in Fig. 8(a and b), together with the corresponding results for the single RBC simulated in Section 4.2. As the pair of RBCs pass close to each other, they are displaced in the positive or negative y direction and the rotational behavior is changed. When the distances between the RBC centers are less than approximately 10 μm, the influences of the interceptions on both transverse movement and rotational behavior are considerable. While displaced by Δx = 70 μm in the x direction, the upper left RBCs (RBC A) with g_{yo} = 3.53 μm, g_{yo} = 5.28 μm and g_{yo} = 7.82 μm are shifted in the y direction by Δy = 1.20 μm, 0.37 μm and 0.62 μm, respectively, and rotated by $\Delta\theta$ = 541 °, 426 ° and 295 °, respectively. Fig. 8(c and d) shows the effect of the initial distance between the two RBC centers in the y direction on the transverse shift and rotation behavior. These results imply that the RBC behavior depends not only on the distance between the two RBC centers in the y direction, but also on the interactive motions of the two RBCs and the surrounding fluid.

Three simulations are carried out to investigate the influence of different initial inclination angles on the intercepting characteristics. In these simulations, the initial inclination angles of the lower right RBCs (RBC B) are θ_{B0} = π/4, π/2 and 3π/4 with the initial inclination angle of the upper left RBCs (RBC A) all set to θ_{A0} = 0 ° (Fig. 1 and Fig. 9). In each case, the two RBCs are separated in the x direction by g_{x0} = 70 μm and in the y direction by g_{y0} = 3.53 μm.

The sequence of evolving motions is depicted in Fig. 9 in the same format as in Fig. 7. (For a better understanding, these results can be considered together with the results for g_{x0} = 70 μm, g_{y0} = 3.53 μm and $\theta_{A0} = \theta_{B0}$ = 0 ° shown in Fig. 7(a)) In each case, the pair of RBCs is not distributed symmetrically with respect to the origin, showing different inclination angles at the same instant because of the different initial inclination

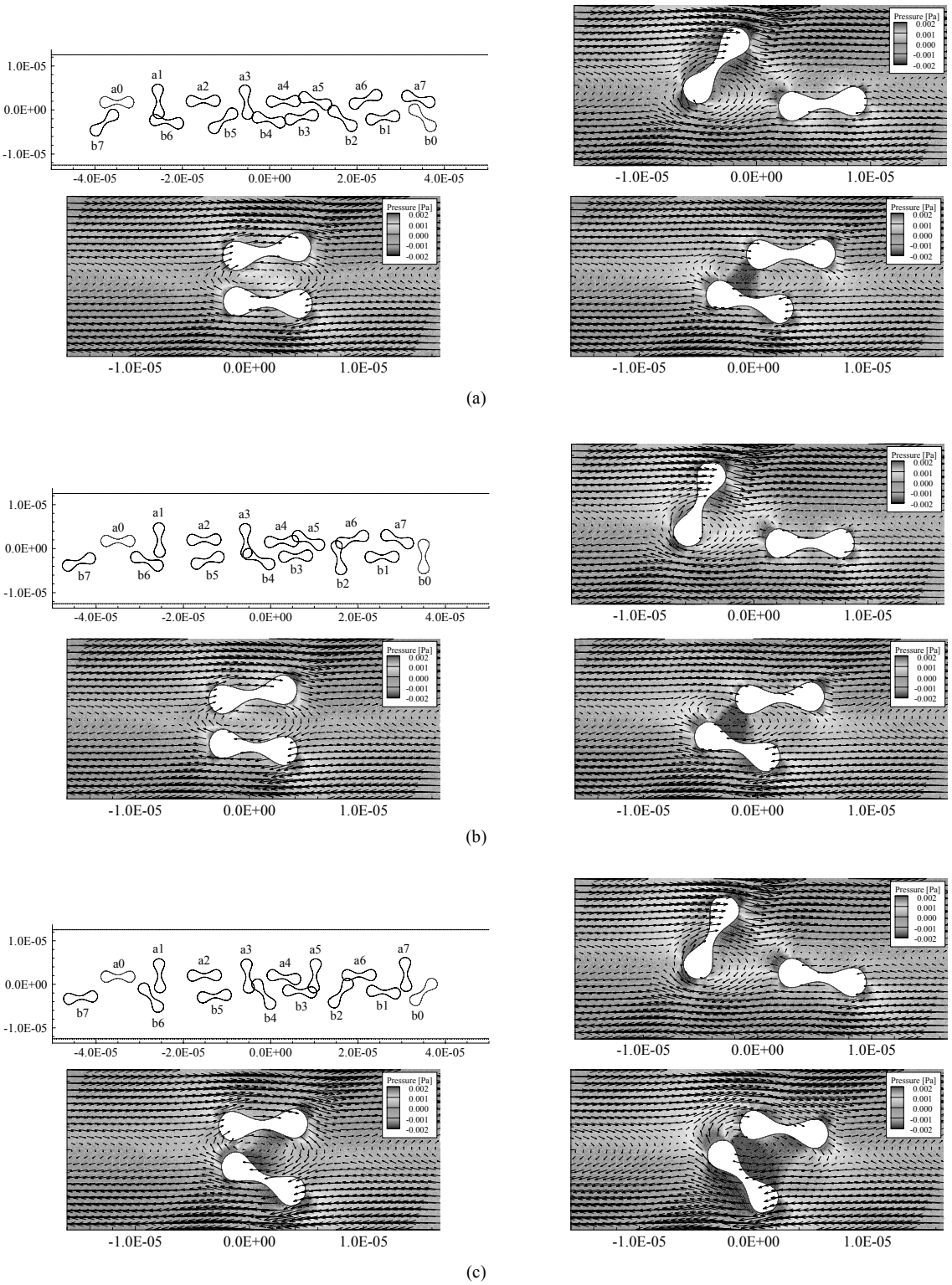

Fig. 9. Time sequence of evolving configurations of three pairs of RBCs with different initial inclination angles (θ_{B0}) for θ_{A0} = 0 °, g_{x0} = 70 μm and g_{y0} = 3.53 μm. (a) $\theta_{B0} = \pi/4$, (b) $\theta_{B0} = \pi/2$, and (c) $\theta_{B0} = 3\pi/4$. The first figures show evolving configurations. The other snapshots show the velocity vectors and pressure distributions ((a): $t^* = \dot{\gamma}t$ = 16.08, 19.08 and 20.08, (b) t^* = 15.56, 18.56 and 19.56, (c) t^* = 15.68, 18.69 and 19.68).

angles of the two RBCs and the RBCs pass each other without collision. It is notable that although the RBC Bs are initially placed at different inclination angles in the three cases, the intercepting characteristics shown in Fig. 7(a) and Fig. 9 are similar. These results mean that the rotational behaviors of the approaching RBCs are adjusted by interacting with the sur-

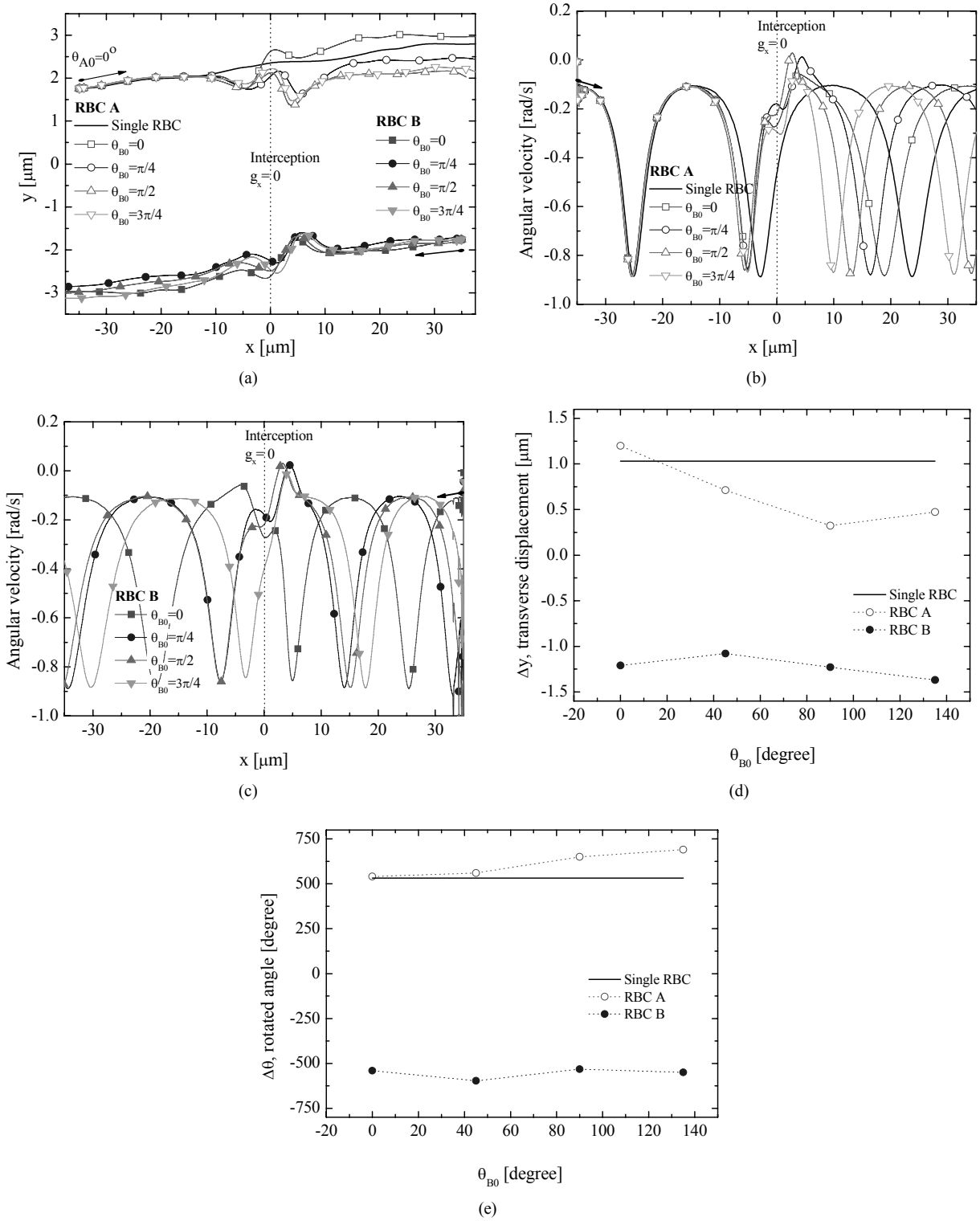

Fig. 10. Behavior of three pairs of RBCs intercepting with different initial inclination angles (θ_{B0}) for θ_{A0} = 0 °, g_{x0} = 70 μm and g_{y0} = 3.53 μm. (a) Trajectories of the centers of the RBCs. (b) Variations of the angular velocities of RBC A. (c) Variations of the angular velocities of RBC B. (d) and (e) are net transverse displacements and rotated angles, respectively, after the RBCs are displaced by 70 μm along the x axis.

rounding flow fields.

Fig. 10(a, b and c), depicting the trajectories of the RBC centers and the angular velocities, shows that the transverse motions of the RBCs as well as the angular velocities are adjusted when the distances between the RBC centers are within about 30 μm. The effects of interception on the transverse

displacements and rotation angles are different, as shown in Fig. 10(d and e). When displaced by Δx = 70 μm in the x direction, the upper left RBCs (RBC A) with initial inclination angles of $\pi/4$, $\pi/2$ and $3\pi/4$ are shifted to the y direction by Δy = 0.71 μm, 0.32 μm and 0.47 μm, respectively, and rotated by $\Delta\theta$ = 560 º, 650 º and 690 º, respectively. The lower right RBCs (the RBC B) with the above three different inclination angle are displaced in the y direction by Δy = 1.08 μm, 1.23 μm and 1.37 μm, respectively, and rotated by $\Delta\theta$ = 597 º, 532 º and 550 º, respectively. Motions in the positive and negative y directions found during the interception are the result of the time series of instantaneous forces exerted by the shear stresses and pressures on the RBC surfaces, which may be attractive or repulsive [30].

5. Conclusions

Direct numerical simulations of the motions of RBCs freely suspended in shear flow have been performed to illustrate the nature of interception of a pair of RBCs, using a fluid-particle interaction method based on the arbitrary Lagrangian-Eulerian (ALE) method and the dynamic mesh method. Here, the governing equations for the fluid flow and red blood cell (RBC) motion are sequentially solved in a two-way coupling fashion. The overall calculation procedure is entirely implemented by a fluid-particle interaction algorithm. We validated the method by comparing simulation results with analytical solutions for the motion of an elliptical particle in shear flow. The comparison showed that the present numerical methods are applicable to the fluid-particle interaction problems.

The results show that both the individual behavior of an RBC and the interception of a pair of RBCs interact with the surrounding fluid flow. The results of simulations show that during the interception, transverse shifts of the RBCs take place, yielding a non-zero RBC self-diffusivity, and a phase shift in the RBC rotation occurs and lasts after the interception. In addition, lower and higher pressures generated locally between the two RBCs cause attractive and repulsive forces between the RBCs yielding transverse displacements and affecting rotation. The results of the present study demonstrate that the behaviors of RBCs approaching each other are adjusted by interaction with the surrounding flow fields during the interception. In summary, the nature of the pairwise interception depends not only on the flow fields generated near the RBCs, but also on the time series of the distance between the two RBC centers and the difference in the inclination angles and kinematic characteristics including translational and rotational behavior. To our knowledge, this is the first attempt to simulate RBC interception using a fluid-particle interaction method.

In human blood flow with normal hematocrit (about 38-46 %), the interceptions between RBCs or blood cells will occur frequently. At the same time, the flows near RBCs will be seriously disturbed and the pressures will be irregularly perturbed. In such circumstances, the RBCs are randomly displaced and rotated in a non-periodic pattern. As a result, such a frequent interception of RBCs has an effect on the effective viscosity of the blood in bulk. Therefore, it would be very meaningful to estimate the self-diffusivity of RBCs in the interceptions among a number of RBCs in order to investigate the effect on effective viscosity. Efforts in the near future are directed toward investigation of the properties of bulk liquid including suspensions of RBCs. The insights on computational and physical issues extracted from the present work will serve as a guide in future endeavors.

References

[1] H. H. Hu, Direct simulation of flows of solid-liquid mixtures, *Int. J. Multiphase Flow,* 22 (1996) 335-352.

[2] J. J. Feng, P. Huang and D. D. Joseph, Dynamic simulation of sedimentation of solid particles in an Oldroyd-B fluid, *J. Non-Newtonian Fluid Mech.,* 26 (1996) 63-88.

[3] H. H. Hu, M. Y. Zhu and N. Patankar, Direct numerical simulations of fluid solid systems using the arbitrary Lagrangian Eulerian technique, *J. Comput. Phys.,* 169 (2001) 427-462.

[4] T. Gao and H. H. Hu, Deformation of elastic particles in viscous shear flow, *J. Comput. Phys.,* 228 (2009) 2132-2151.

[5] R. Lima, T. Ishikawa, Y. Imai, M. Takeda, S. Wada and T. Yamaguchi, Radial dispersion of red blood cells in blood flowing through glass capillaries: The role of hematocrit and geometry, *J. Biomech.,* 41 (2008) 2188-2196.

[6] G. B. Jeffery, The Motion of ellipsoidal particles immersed in a viscous fluid. *Proceedings of the Royal Society of London. Series A*, Containing papers of a mathematical and physical character, 102 (1922) 161-179.

[7] S. R. Keller and R. Skalak, Motion of a tank-treading ellipsoidal particle in a shear flow, *J. Fluid Mech.,* 120 (1982) 27-47.

[8] F. Rioual, T. Biben and C. Misbah, Analytical analysis of a vesicle tumbling under a shear flow, *Phys. Rev. E: Stat. Phys. Plasmas Fluids,* 69 (2004) 061914.

[9] M. Abkarian, M. Faivre and A. Viallat, Swinging of red blood cells under shear flow, *Phys. Rev. Lett.,* 98 (2007) 188302.

[10] J. M. Skotheim and T. W. Secomb, Red blood cells and other non-spherical capsules in shear flow: Oscillatory dynamics and the tank-treading-to-tumbling transition, *Phys. Rev. Lett.,* 98 (2007) 078301.

[11] R. R. Huilgol and N. Phan-Thien, *Fluid Mechanics of Viscoelasticity*, *Elsevier*, Amsterdam, (1997).

[12] D. I. Dratler and W. R. Schowalter, Dynamic simulation of suspensions of non-Brownian hard spheres, *J. Fluid Mech.,* 325 (1996) 53-77.

[13] D. I. Dratler, W. R. Schowalter and R. L. Hoffman, Dynamic simulation of shear thickening in concentrated colloidal suspensions, *J. Fluid Mech.,* 353 (1997) 1-30.

[14] J. J. Stickel and R. L. Powell, Fluid mechanics and rheology of dense suspensions, *Ann. Rev. Fluid Mech.,* 37 (2005)

129-149.
[15] N. Phan-Thien, X. J. Fan, R. I. Tanner and R. Zheng, Folgar-Tucker constant for a fiber suspension in a Newtonian fluid, *J. Non-Newtonian Fluid Mech.,* 103 (2002) 251-260.
[16] S. Chandrasekhar, *Liquid crystals*, *Cambridge University Press*, Cambridge, (1992).
[17] M. Doi and S. F. Edwards, *The theory of polymer dynamics*, *Oxford University Press*, New York, (1986).
[18] B. J. Yoon and S. Kim, A boundary collocation method for the motion of two spheroids in Stokes flow; hydrodynamic and colloidal interaction, *Int. J. Multiphase Flow,* 16 (1990) 639-649.
[19] C. J. S. Petrie, The rheology of fibre suspensions, *J. Non-Newtonian Fluid Mech.,* 87 (1999) 369-402.
[20] C. Pozrikidis, Orientation statistics and effective viscosity of suspensions of elongated particles in simple shear flow, *Eur. J. Mech. B. Fluids,* 24 (2005) 125-136.
[21] C. Pozrikidis, Interception of two spheroidal particles in shear flow, *J. Non-Newtonian Fluid Mech.,* 136 (2006) 50-63.
[22] E. A. Evans and R. Skalak, editors. *Mechanics and thermodynamics of biomembranes*, *CRC Press*, Boca Raton, FL, (1980).
[23] J. Li, M. Dao, C. T. Lim and S. Suresh, Spectrin-level Modeling of the cytoskeleton and optical tweezers stretching of the erythrocyte, *Biophys. J.,* 88 (2005) 3707-3719.
[24] R. Skalak and S. Chien, *Handbook of Bioengineering*, *McGraw-Hill*, New York, (1987).
[25] FLUENT 6.3 documentation, ANSYS.
[26] S. R. Keller, *A model for erythrocyte tank-treading motion in a shear flow*. In 1979 Advances in Bioengineering (ed. M. K. Wells), *A.S.M.E.,* (1979) 125-127.
[27] C. Migliorini, Y. Qian, H. Chen, E. B. Brown, R. K. Jain and L. L. Munn, Red blood cells augment leukocyte rolling in a virtual blood vessel, *Biophys. J.,* 83 (2002) 1834-1841.
[28] C. Sun, C. Migliorini and L. L. Munn, Red blood cells initiate leukocyte rolling in postcapillary expansions: A lattice Boltzmann analysis, *Biophys. J.,* 85 (2003) 208-222.
[29] C. Sun, L. L. Munn, Lattice-Boltzmann simulation of blood flow in digitized vessel networks, *Computers and Mathematics with Applications,* 55 (2008) 1594-1600.
[30] B. Neu and H. J. Meiselman, Depletion-mediated red blood cell aggregation in polymer solutions, *Biophys. J.,* 83 (2002) 2482-2490.

Choeng Ryul Choi is researching at the Department of Mechanical Engineering, College of Engineering, Kyung Hee University. He is interested in computational fluid dynamics, fluid-structure interaction, and physics of complex system

Chang Nyung Kim is a full professor of the Department of Mechanical Engineering, College of Engineering, Kyung Hee University in the Republic of Korea. His research focuses on computational fluid dynamics, micro-fluidic flow, heat transfer, biomechanics, and environmental fluid mechanics.